High-Utilisation Nanoplatinum Catalyst (Pt@cPIM) Obtained via Vacuum Carbonisation in a Molecularly Rigid Polymer of Intrinsic Microporosity

REVISION

30th November 2016

High-Utilization Nano-Platinum Catalyst (Pt@cPIM) Obtained via Vacuum Carbonization in a Molecularly Rigid Polymer of Intrinsic Microporosity

---

Yuanyang Rong [1], Daping He [1], Richard Malpass-Evans [2], Mariolino Carta [2], Neil B. McKeown [2], Murilo F. Gromboni [3], Lucia H. Mascaro [3], Geoffrey W. Nelson [4], John S. Foord [5], Philip Holdway [6], Sara E.C. Dale [7], Simon Bending [7], and Frank Marken *[1]

[1] *Department of Chemistry, University of Bath, Claverton Down, Bath BA2 7AY, UK*
[2] *EastChem School of Chemistry, University of Edinburgh, David Brewster Road, Edinburgh, EH9 3FJ, UK*
[3] *Department of Chemistry, Federal University of São Carlos, Rod. Washigton Luiz, km235, CEP 13565-905, São Carlos, SP – Brazil*
[4] *Imperial College London, Department of Materials, Royal School of Mines, Exhibition Road, London, SW7 2AZ, UK*
[5] *Chemistry Research Laboratories, Oxford University, South Parks Road, Oxford OX1 3TA, UK*
[6] *Department of Materials, Oxford University, Begbroke Science Park, Begbroke Hill, Oxford OX5 1PF, UK*
[7] *Department of Physics, University of Bath, Claverton Down, Bath BA2 7AY, UK*

To be submitted to Electrocatalysis

Email f.marken@bath.ac.uk

Abstract

Polymers of intrinsic microporosity (PIM or here PIM-EA-TB) offer a highly rigid host environment into which hexachloroplatinate(IV) anions are readily adsorbed and vacuum carbonized (at 500 °C) to form active embedded platinum nanoparticles. This process is characterised by electron and optical microscopy, AFM, XPS, and electrochemical methods, which reveal that the PIM microporosity facilitates the assembly of nanoparticles of typically 1.0-2.5 nm diameter. It is demonstrated that the resulting carbonized "Pt@cPIM" from drop-cast films of ca. 550 nm average thickness, when prepared on tin-doped indium oxide or ITO, contain fully encapsulated but also fully active platinum nanoparticles in an electrically conducting heterocarbon host. Alternatively, for thinner films (50-250 nm) prepared by spin-coating, the particles become more exposed due to additional loss of the carbon host. In contrast to catalyst materials prepared by vacuum-thermolyzed hexachloroplatinate(IV) precursor, the platinum nanoparticles within Pt@cPIM retain high surface area, electrochemical activity, and high catalyst efficiency due to the molecular rigidity of the host. Data are presented for oxygen reduction, methanol oxidation, and glucose oxidation and in all cases the high catalyst surface area is linked to excellent catalyst utilization. Robust transparent platinum-coated electrodes are obtained with reactivity equivalent to bare platinum but with only 1 μg Pt cm^{-2} (i.e. ~ 100% active Pt nanoparticle surface is maintained in the carbonised microporous host).

Key words: fuel cell; noble metal; nanocatalyst; one-step synthesis; encapsulation; voltammetry

1. Introduction

The preparation and formulation of catalysts for applications in fuel cells [1] and in sensors [2] remain a highly active research topic. For example, the development of new types of porous substrate materials [3] offer catalysts with (i) better levels of performance [4,5], (ii) improved access into a wide range of reproducible and highly efficient catalyst composites [6], and/or (iii) access to more sustainable catalyst systems [7]. Many new inorganic [8] or carbon-based catalyst composite materials [9,10] are under development and, in particular, synthetic methods based on the carbonization of precursors to yield carbon-embedded catalysts [11,12] have proved beneficial. Novel and highly efficient types of carbon-embedded platinum catalysts have been obtained via carbonization [13]. However, directly embedding active nano-platinum catalysts without loss of activity during carbonization in a one-step procedure is uncommon and desirable.

Platinum nanoparticles are the basis for the overwhelming majority of technical catalyst systems due to the durability of platinum and due to the special place platinum takes with respect to interfacial adsorption of reaction intermediates [14]. Platinum nanoparticles are employed in PEM fuel cells [15], in methanol [16] and glucose [17] driven fuel cells, but also in many dye-sensitised solar cells [18] and in electrolysers for energy conversion [19]. The most active size range for platinum has been reported to be 2-6 nm (based on mass activity) [20]. However, the catalyst durability and corrosion characteristics are also important [21]. We have recently demonstrated that a new class of polymers with intrinsic microporosity (PIMs) can be employed to stabilise Pt nanoparticle performance for both anode and cathode activity [22,23].

Platinum nanoparticles provide very effective catalysts but suffer from high cost of the non-sustainable noble metal catalyst. Therefore, intense research efforts are directed towards either replacing platinum with cheaper and more sustainable metals (e.g. based on alloys of Fe, Co, Ni, etc. [24]) or improving utilisation. The latter involves maximising the surface area and reactivity of platinum, for example, by embedding nanoparticles into porous hosts or substrates [25]. Porous polymer materials are emerging as promising substrates (or precursors for porous substrates) for the immobilisation and growth of platinum nano-catalysts [26]. Highly porous polymer structures that can retain microporosity during carbonization are particularly interesting. For PIM materials it has been suggested that carbonization occurs via cross-linking and without breaking the of the rigid polymer backbone strands [27].

Polymers of intrinsic microporosity (or PIMs [28]) exhibit micropore diameter of typically 0.5-2.0 nm and N_2-adsorption surface area values up to 1000 m^2g^{-1} [29]. They were originally developed for gas storage [30] and separation [31], but recently have also proven utility for electrochemical processes such as electrocatalysis [32], ionic devices [33], or electroanalysis [34]. Most work in PIM electrochemistry to date has been carried out with PIM-EA-TB (prepared from a diaminoethanoanthracene "EA" monomer polymerised via a Tröger base "TB" coupling; see structure in Figure 1). This polymer with highly rigid molecular structure exhibits N_2-adsorption surface area of 1027 m^2g^{-1} and is employed here with molecular weight of 70 kDa [33].

We have demonstrated previously that relatively gentle vacuum carbonization of PIM-EA-TB at 500 °C causes conversion of the microporous starting material into a microporous conducting hetero-carbon [27]. Although the electrical conductivity of the new carbon material was limited,

thin films deposited onto tin-doped indium oxide (ITO) substrates were clearly capacitive and suitable for application as high surface area carbon film electrodes. A key feature in the conversion of PIM-EA-TB to the carbonized form (cPIM) is the retention of structural porosity/integrity. There were no changes in cumulative pore volume and no apparent changes in morphology upon vacuum carbonization [27]. Therefore, this hetero-carbon formation may offer ideal conditions for the co-formation/embedding of nano-catalysts with the following advantages: (A) the rigid PIM-EA-TB does not block/affect the catalytically active Pt particle surface and (B) after carbonization, porosity and connectivity are maintained to allow electrical contact and sufficient access for reactants to the active catalyst surface.

Here, we add a well-defined amount of platinum pre-cursor ($PtCl_6^{2-}$) by absorption into the porous protonated form of PIM-EA-TB and during subsequent vacuum carbonisation nano-particulate platinum is formed *in-situ* and without encapsulation or blocking of the active catalyst surface (Figure 1). The microporous hetero-carbon host surrounding the platinum nano-catalyst ensures good electrical connection and therefore excellent catalyst utilisation.

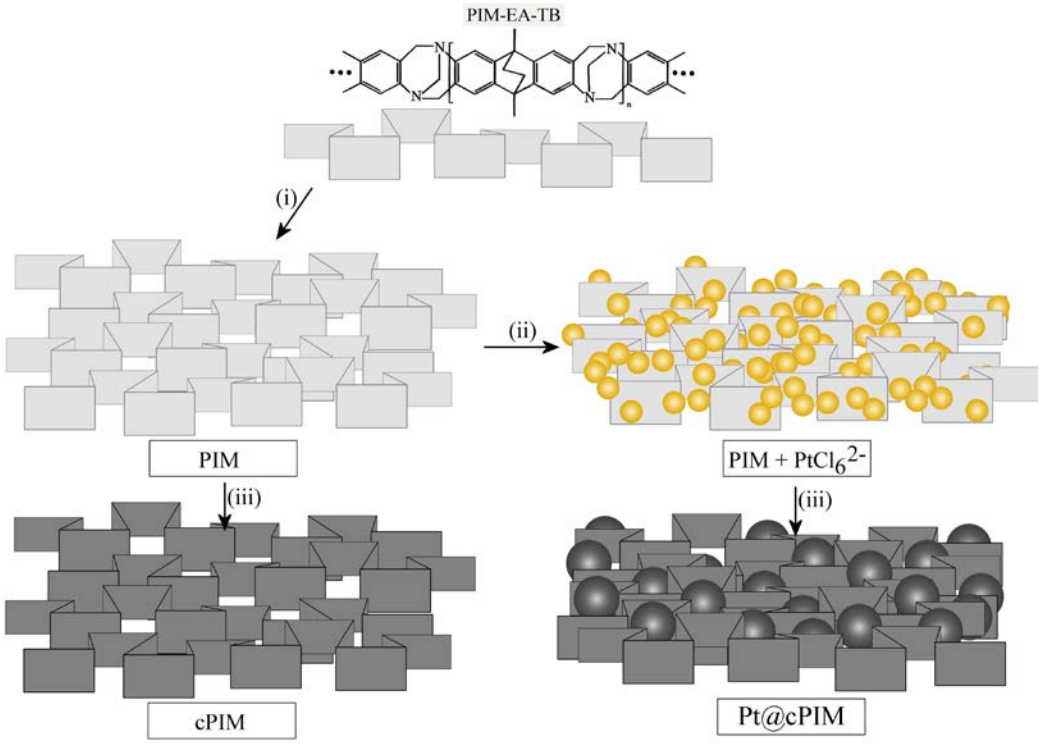

Figure 1. Schematic representation of (i) the formation of a film of PIM-EA-TB, (ii) absorption of $PtCl_6^{2-}$ into the film, and (iii) vacuum carbonisation at 500 °C to give highly porous hetero-carbon materials with/without nano-platinum catalyst.

It is shown that PIM-EA-TB as a precursor host material can be employed to generate/maintain platinum nanoparticle size (at typically 1.0-2.5 nm) and to improve nano-catalyst performance by building up thicker layers of catalyst (with additive performance). Catalysts are prepared in a simple one-step vacuum carbonization process in which the PIM-EA-TB polymer is converted into an electrically conducting host (of similar porosity) containing the platinum nanoparticle catalyst in a way that it is accessible to the solution phase. In contrast to solution casting, spin-coating produces thinner films which, when carbonized, give highly effective platinum catalyst layers on transparent tin-doped indium oxide (ITO) electrode surfaces.

2. Experimental

2.1. Chemical Reagents

Dipotassium platinum(IV)hexachloride, D-(+)-glucose, phosphoric acid (85%), sodium hydroxide, perchloric acid (96%), sodium chloride and hydrochloric acid (30%) were purchased in analytical grade from Aldrich or Fisher Scientific and used without further purification. PIM-EA-TB was prepared following the literature procedure [35]. All solutions were prepared using deionized water (resistivity 18 MOhm cm at 22 °C) from a Thermo Scientific water purification system.

2.2. Instrumentation

Heating was performed in a TSH12 tube furnace (Elite Thermal System Ltd.). Pt nanoparticle materials were characterised by transmission electron microscopy (TEM) on a Jeol 1200EXII TEM system (with EDS and STEM). All electrochemical measurements were performed using an Ivium Compactstat potentiostat (The Netherlands) with platinum wire counter electrode and KCl-saturated calomel reference electrode (SCE, Radiometer REF401). The working electrode was prepared from ITO coated glass (tin-doped indium oxide films sputter-coated onto glass, active area 15 mm × 15 mm, resistivity ca. 15 Ω per square) obtained from Image Optics Components Ltd (Basildon, Essex, UK). XPS data were obtained on a Kratos Axis Ultra DLD system using a fixed anode monochromatic Al Kα X-ray source operating at 120 W.

2.3. Preparation of Thick Film Pt@cPIM on Tin-Doped Indium Oxide (ITO)

An aqueous platinum precursor solution was prepared by dissolving 10 mM K_2PtCl_6 in 0.5 M HCl (this solution was unstable as indicated by a slow colour change from yellow to orange and therefore stored in the dark at 4 ºC). A tin-doped indium oxide (ITO) electrode was coated with 60 μL (1 mg/mL in chloroform) PIM-EA-TB in a drop-cast process giving approximately in average 550 nm thick deposits. Next, the ITO with PIM-EA-TB layer was dipped into the platinum precursor solution for 5 minutes (to allow sufficient time for ion exchange), then rinsed with water, and dried under ambient conditions. The colour changed from clear to yellow. After the $PtCl_6^{2-}$ impregnation step, the ITO electrode was subjected to vacuum carbonization under oil pump vacuum (ca. 0.1 mTorr) in a quartz tube to fit the tube furnace at 500 °C for 3 h to obtain cPIM-Pt with embedded platinum nanoparticles. Elemental analysis (Butterworth Analytical Laboratories, London) was performed for two samples: (A) for PIM-EA-TB treated with $Pt(IV)Cl_6^{2-}$: Pt 6.8% C 55.5% H 5.2% N 6.2% and (B) for cPIM-Pt: Pt 10.2% C 72.4% H 2.1% N 5.7%. Residual mass is likely to be associated with inorganic components such as KCl. Note that in the ratio of platinum atoms to nitrogen atoms in PIM-EA-TB treated with $Pt(IV)Cl_6^{2-}$ is 0.08 (or 8%), which suggests that only partial loading of the polymer was achieved.

2.4. Preparation of Thin Film Pt@cPIM on Tin-Doped Indium Oxide (ITO)

PIM-EA-TB was dissolved in chloroform to prepare solutions with four different concentrations (0.25%, 0.5%, 1% and 2% wt.). Spin-coating of these solutions (WS-650Mz-23NPP (Laurell Technologies) using a rotation rate of 1500 rpm for 1 minute and ITO substrates of 15 mm × 15 mm area resulted in different thicknesses of PIM-EA-TB (*vide infra*). Next, the coated electrode was immersed into the platinum precursor solution (as before) for 5

minutes, then rinsed with water and dried under ambient conditions. Then the ITO electrode was transferred to vacuum carbonization under oil pump vacuum (Edwards, ca. 0.1 mTorr) in a quartz tube at 500 °C for 3 h to give Pt@cPIM thin films with platinum nanoparticles embedded.

3. Results and Discussion

3.1. Formation and Characterisation of Thick Film Pt@cPIM

Drop-casting was employed with 60 μL of a PIM-EA-TB solution in chloroform (1 mg/mL) applied to an ITO electrode. With the measured film density of 1.1 g cm^{-3} for PIM-EA-TB [36] this allows an average film thickness to be estimated as 550 nm. With platinum bound into the film (see elemental analysis results in the experimental section) a coverage of about 6 μg Pt cm^{-2} is anticipated. Under $PtCl_6^{2-}$ absorption conditions employed here only approximately 8% of the nitrogen atoms in the polymer are associated with a platinum. The vacuum carbonization process when applied to a film of PIM-EA-TB on an ITO substrate is known to produce a nitrogen-containing hetero-carbon with significant electrical conductivity, the characteristic Raman signature for a graphitic structure, retained cumulative pore volume/morphology and the black coloration of carbon [27]. The N_2 adsorption data for PIM-EA-TB suggests a surface area of 1027 m^2 g^{-1} before carbonization [33] and 242 m^2 g^{-1} after carbonization [27].

Here, PIM-EA-TB only is vacuum carbonized to give cPIM and with absorbed $PtCl_6^{2-}$ in the porous structure to give Pt@cPIM. Figure 2 shows transmission electron micrographic (TEM) evidence for the presence of cPIM carbon material and for the embedded Pt nanoparticles in Pt@cPIM (contrast Figures 2A and 2B). Higher magnification (Figure 2C and 2D) allows

individual particles (black or grey) to be analysed and the average particles size to be estimated as typically 1.0-2.5 nm. This value is similar to the micropore size for the PIM-EA-TB polymer starting material (from N_2 gas adsorption isotherm data [33]). Electron diffraction data (Figure 2E and 2F) clearly confirm that the carbonization process leads to inclusion of platinum nanoparticles. The diffraction rings are consistent with Pt(331), Pt(222), Pt(311), Pt(220), Pt(200), and Pt(111) (compare JCPDS 4-0802 structure information [37]).

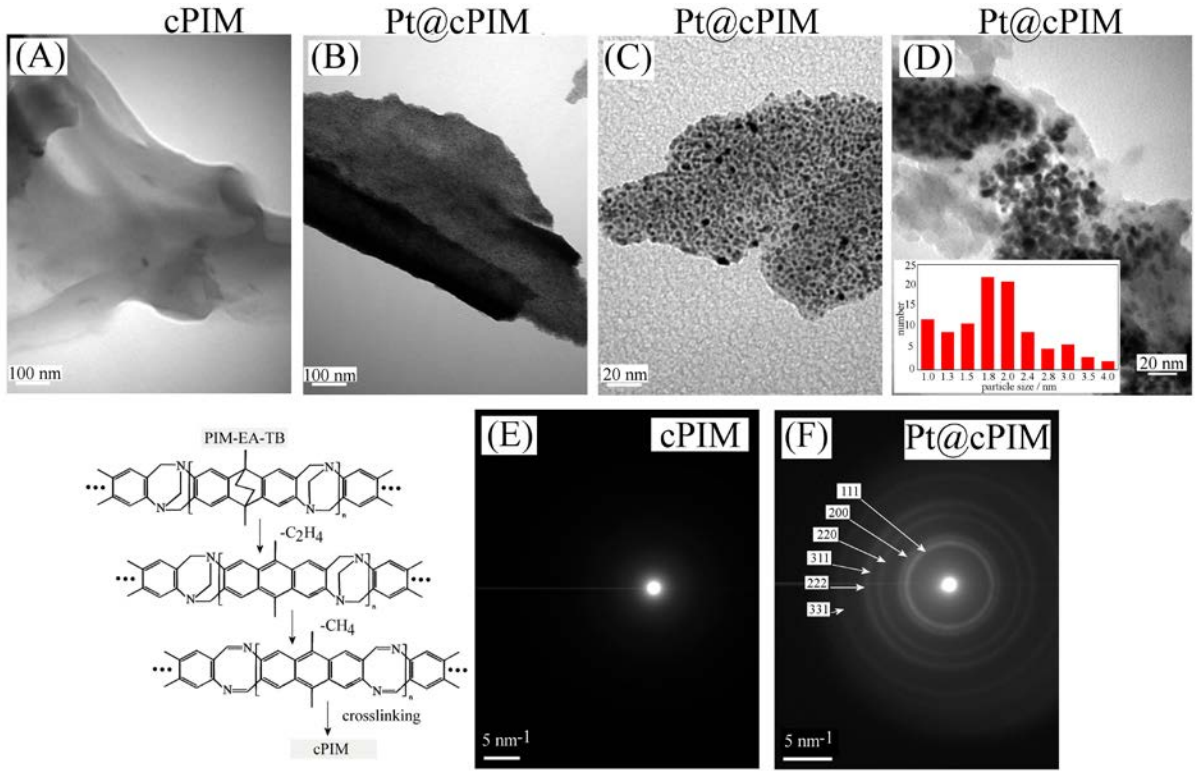

Figure 2. Transmission electron micrographs for (A) thick cPIM, (B) thick Pt@cPIM, (C) thick Pt@cPIM, and (D) thin film Pt@cPIM with particle size analysis. Also shown is a schematic reaction pathway for carbonization and diffraction pattern for (E) cPIM and (F) Pt@cPIM.

3.2. Formation and Characterisation of Thin Film Pt@cPIM

When employing spin-coating instead of drop-casting, better defined coatings of PIM-EA-TB can be produced. By changing the wt% or PIM-EA-TB in chloroform and keeping the spin

coating conditions constant (see experimental) film thickness can be varied from about 50 to 250 nm (based on AFM cross-sectional data, see Figure D). These films are more uniform compared to deposits formed by drop-casting. AFM images of bare ITO and cPIM coated ITO are shown in Figure 3A and 3B consistent with a uniform coating. Perhaps surprisingly, when $PtCl_6^{2-}$ is absorbed into the PIM deposit prior to vacuum-carbonization, the morphology is affected and only thinner deposits seem to remain (see the more apparent substrate grain boundaries in Figure 3C). This observation is confirmed by SEM imaging.

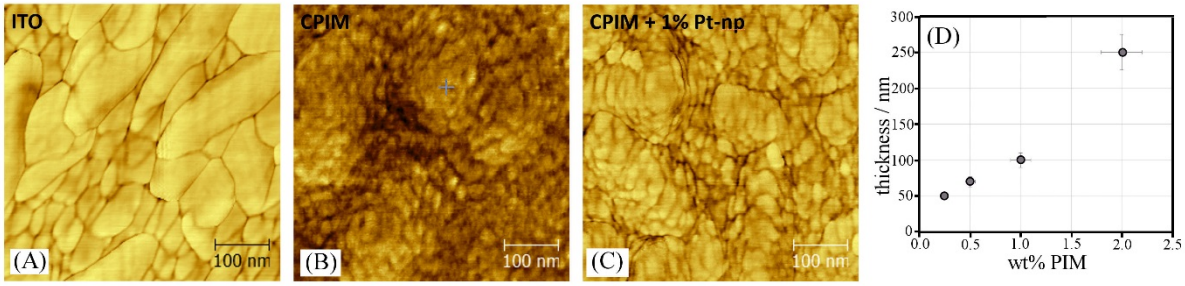

Figure 3. Atomic force microscopy (AFM) images for (A) bare ITO, (B) cPIM-coated (1 wt%) ITO, and (C) Pt@cPIM (1 wt%) coated ITO. (D) Plot of cross-sectional height data for 0.25 wt%, 0.5 wt%, 1 wt%, and 2 wt% PIM-EA-TB in chloroform employed for spin coating.

Figure 4 shows both cross-sectional and morphological SEM images for different types of spin-coated PIM deposits on ITO. The PIM film in Figure 4A is formed from 1 wt% PIM in chloroform with an approximately 100 nm thin film clearly visible (containing $PtCl_6^{2-}$ as "stain"). Films of vacuum-carbonized PIM (without Pt) also form well-defined films (Figure 4B). However, when exploring cross-sectional images of 1 wt% and 2 wt% PIM films with $PtCl_6^{2-}$ immobilised, it is apparent that a part of the carbon deposit is missing (removed by the vacuum carbonization process).

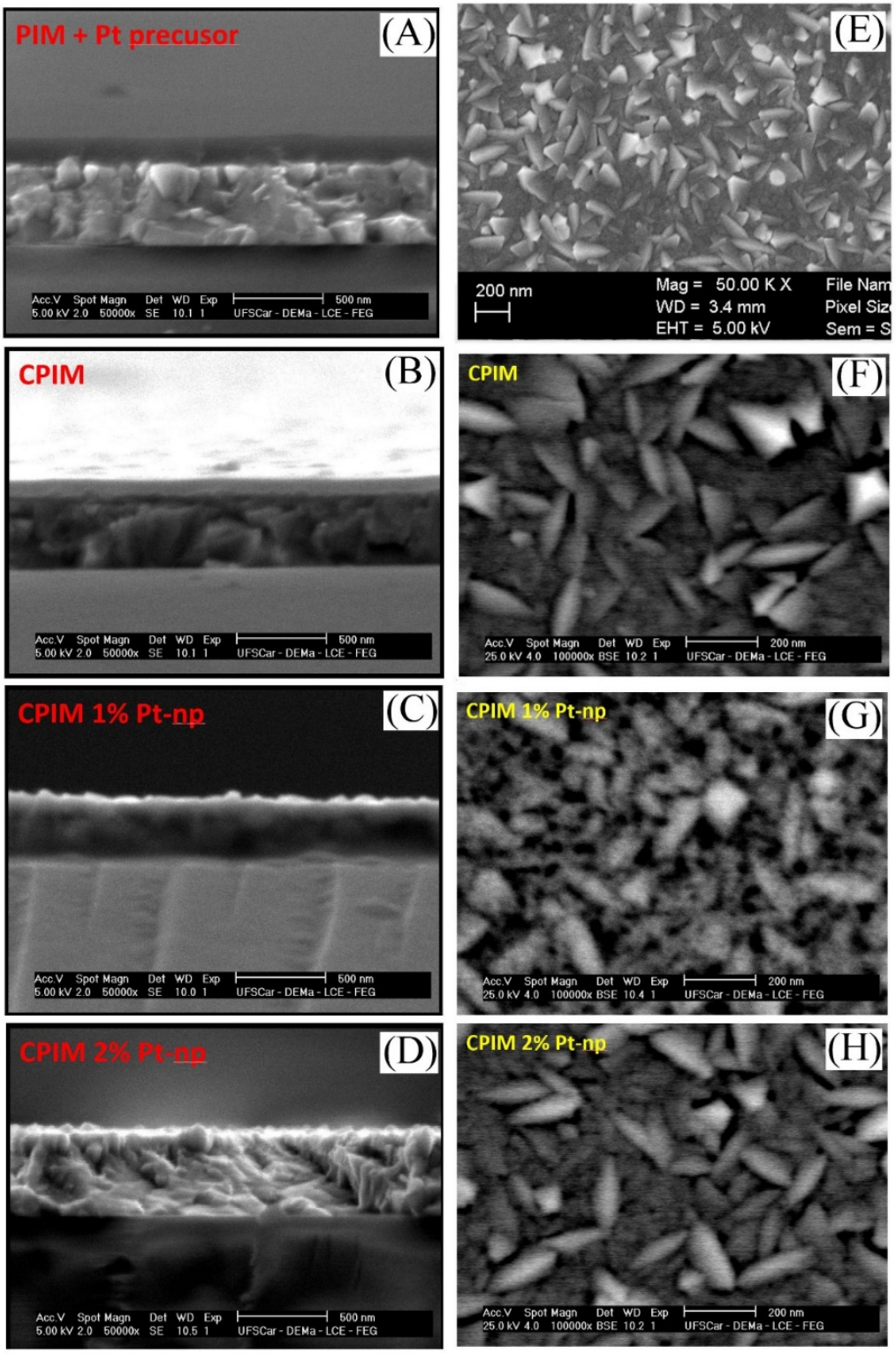

Figure 4. Cross-sectional scanning electron microscopy (SEM) images for (A) PIM-Pt (spin-coated from 1 wt%), (B) cPIM showing the carbonized film without platinum, (C) Pt@cPIM (spin-coated from 1 wt%), and (D) Pt@cPIM (spin-coated from 2 wt%). Loss of carbon material during carbonization for the platinum containing films is evident. Also shown are SEM images for (E) base ITO, (F) cPIM coated ITO, (G) Pt@cPIM (spin-coated from 1 wt%), and (H) Pt@cPIM (spin-coated from 2 wt%).

Additional morphological images (Figure 4G and 4H) show that platinum is present (as nano-structured deposit on top of the ITO crystals), but evidence for the amount of remaining cPIM substrate material is not clear. Next, XPS experiments were performed. Figure 5 shows survey data for PIM and PIM-Pt with the additional Pt signal clearly observed. After vacuum carbonization of a thin film of PIM-EA-TB (from 1 wt% solution), cPIM (Figure 5C) shows features identical to those reported recently [34]. The higher oxygen signals in cPIM compared to PIM are assigned to ingress and reactivity of oxygen after vacuum carbonization when the sample is exposed to the open atmosphere. Nitrogen is present after carbonization, but the level appears lower relative to that for carbon. For the Pt@cPIM film (Figure 5D) significant changes occur and signals from ITO are clearly evident (compared to Figure 5E). Carbon levels are higher compared to the bare ITO sample but lower when compared to the cPIM sample (Figure 5C). Characteristic Pt4f peaks are observed (see insets) with a splitting into 7/2 and 5/2 states. Binding energies for Pt4f in Figure 5B are consistent with the $PtCl_6^{2-}$ precursor [38] and in Figure 5D with metallic platinum nanoparticles (see Table 1) [39].

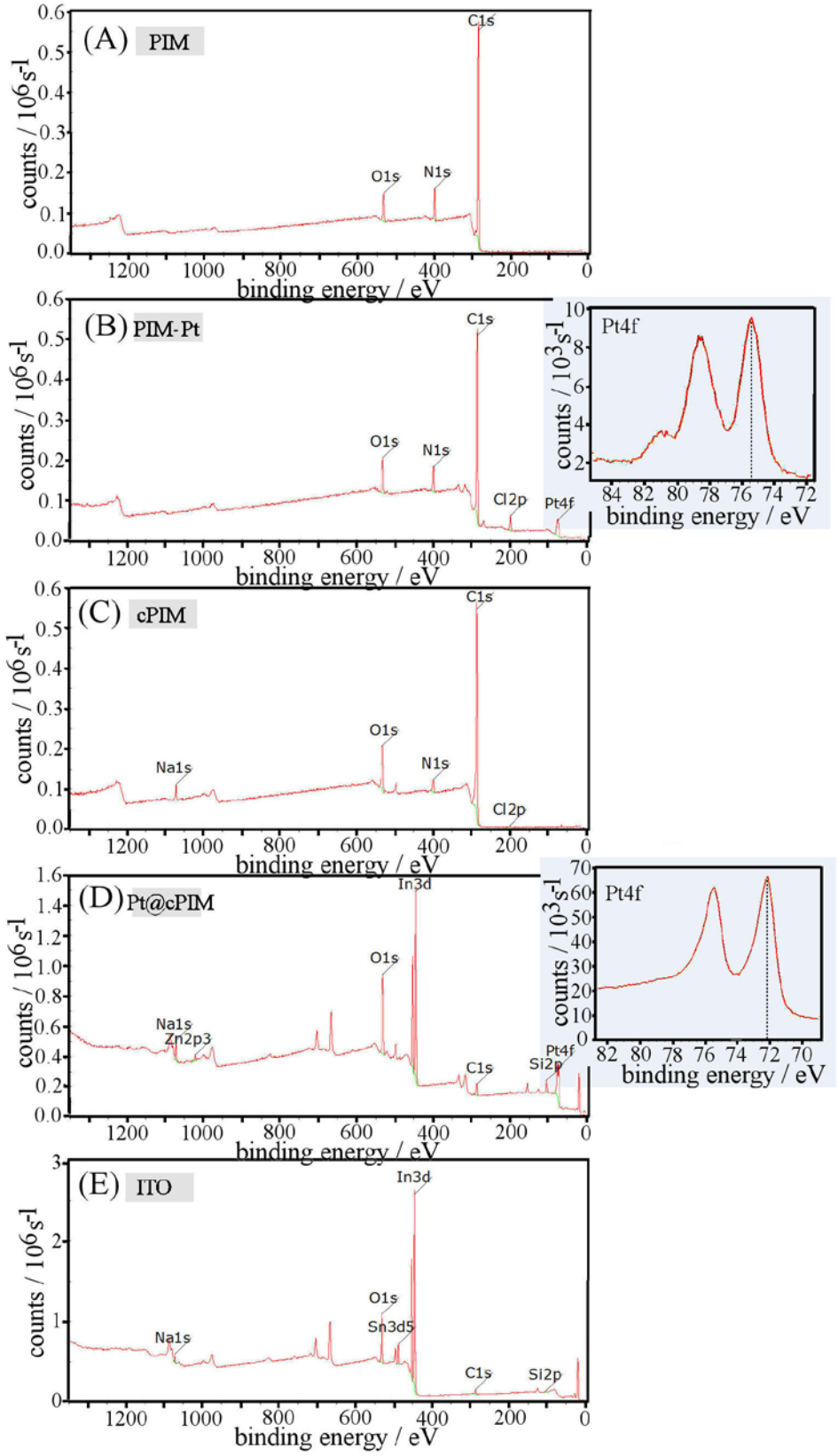

Figure 5. XPS survey spectra for (A) PIM-EA-TB, (B) PIM-EA-TB with Pt precursor absorbed, (C) carbonised PIM, (D) carbonised PIM-EA-TB with Pt precursor, and (E) a bare ITO electrode substrate. Insets show Pt4f data for PIM-Pt and Pt@cPIM.

Table 1. Summary of XPS data for PIM-Pt and Pt@cPIM.

	PIM-Pt		Pt@cPIM	
Element	Peak / eV	At%	Peak / eV	At%
C1s	285.00 [a]	80.94	285.00 [a]	13.42
O1s	532.62	7.77	531.32	51.34
$Pt4f_{7/2}$	75.38	0.79	72.11	4.35

[a] the C1s binding energy was used as reference point with 285.00 eV.

It can be concluded that the vacuum carbonisation of thin film PIM is somewhat affected by the presence of $PtCl_6^{2-}$ (in part possibly due to the formation of volatile carbon halides) but that consistently platinum metal in the form of nanoparticles is formed. Even for the thin film Pt@cPIM deposits, there remains carbon to act as substrate and conductive support for the catalyst. The electrocatalytic reactivity of these materials is investigated next.

3.3. Electrocatalytic Oxygen Reduction

Platinum catalysts are employed widely in fuel cells and particularly in the oxygen reduction reaction [40], which provides an enormous challenge for sustainable production. The reduction of oxygen is reported to be associated mainly with (i) reduction of O_2 to a peroxide intermediate and (ii) further reduction to water (equation 1) [41].

$$O_2(aq) + 2\ H^+(aq) + 2\ e^-(m) \rightarrow H_2O_2(ads) \quad (1a)$$

$$H_2O_2(ads) \leftrightarrow H_2O_2(aq) \quad (1b)$$

$$H_2O_2(ads) + 2\ H^+(aq) + 2\ e^-(m) \rightarrow 2\ H_2O(aq) \quad (1c)$$

Recent work on PIM-EA-TB stabilised platinum catalysts in oxygen reduction processes has been reported where the platinum nanoparticles and the carbon substrate were “protected” against accelerated corrosion [22]. Here, platinum nanoparticles are embedded into a hetero-carbon host with sufficient porosity to allow reagent access to the catalyst and with sufficient electrical conductivity to allow effective potential control. Figure 6A shows cyclic voltammetry data for “thick film” Pt@cPIM catalyst for the reduction of oxygen saturated 0.1 M phosphate buffer pH 7 (trace iii). The reduction peak is detected at about 0.0 V vs. SCE. When comparing with the reduction of 2 mM H_2O_2 in argon-degassed solution a similar reduction response is observed (trace ii) in addition to the voltammetric signal for the corresponding H_2O_2 oxidation. It seems likely that the reduction of oxygen under these conditions occurs predominantly with H_2O as product (4-electron, see equation 1). Figure 6B shows data for the corresponding processes at a 2 mm diameter Pt disk electrode confirming the assigned mechanism.

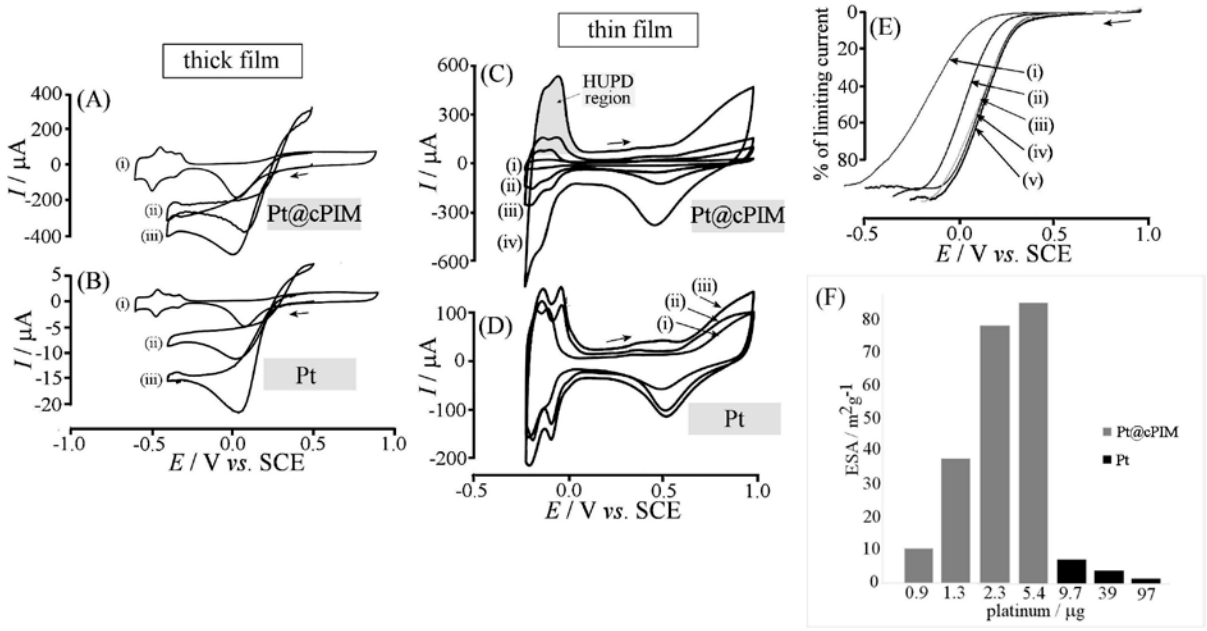

Figure 6. (A) Cyclic voltammograms (scan rate 50 mVs^{-1}; 1 cm^2 thick Pt@cPIM) for (i) argon-degassed solution, (ii) 2 mM H_2O_2, and (iii) oxygen-saturated in 0.1 M phosphate buffer pH 7 for thick film Pt@cPIM. (B) As above for a 2 mm diameter Pt disc electrode. (C) Cyclic voltammograms (scan rate 100 mVs^{-1}; 2.2 cm^2 thin Pt@cPIM) for argon-degassed 0.1 M $HClO_4$ for (i) 0.9, (ii) 1.3, (iii) 2.3, and (iv) 5.4 μg Pt and (D) pure Pt deposits for (i) 9.7, (ii) 39, and (iii) 97 μg Pt. (E) Normalised cyclic voltammograms for the reduction of oxygen in 0.1 M perchloric acid for thin Pt@cPIM (i) 0.9, (ii) 1.3, (iii) 2.3, and (iv) 5.4 μg Pt and (v) for pure Pt deposit 9.7 μg Pt. (F) Plot of electrochemically active surface area (ESA, estimated from HUPD region assuming 210 μC cm^{-2} [42]) versus platinum amount deposited.

Figure 6C shows cyclic voltammetry data obtained with "thin film" Pt@cPIM with increasing film thickness and platinum coverage values of (i) 0.9, (ii) 1.3, (iii) 2.3, and (iv) 5.4 μg cm^{-2} Pt. The surface area of platinum increases systematically with Pt@cPIM film thickness as seen from the hydrogen-UPD region (see Figure 6C) and the oxide region. Similar experiments without PIM were performed by directly depositing H_2PtCl_6 platinum precursor onto ITO and thermal conversion without polymer (Figure 6D). For this set of samples surface area of platinum can be seen to remain well below that observed for Pt@cPIM. Accordingly, the surface area and therefore the catalytic activity/utilisation of Pt@cPIM are improved due to the

templating effect of the microporous polymer. Figure 6E shows data for the reduction of oxygen under gentle hydrodynamic agitation (bubbling oxygen). The catalytic effect of approximately 2.3 μg (or ca. 1 μg cm^{-2}) Pt in Pt@cPIM approaches that of bare platinum.

The electrochemically active surface area (ESA) for platinum nanoparticles was estimated by cyclic voltammetry in 0.1 M $HClO_4$ solution (saturated with argon). Figure 6C shows characteristic peaks for hydrogen adsorption (H_{ads}) at -0.09 V and -0.17 V vs SCE. The ESA value can be calculated by measurement of charge under the hydrogen electro-adsorption curve (Q_H) using equation 2 [43].

$$ESA = \frac{Q_H}{Q_{ref}} = \frac{Q_H}{210\ \mu C\ cm^{-2}} \qquad (2)$$

Data are summarised in Figure 6F. The ESA value for platinum nanoparticles supported on carbonized PIM is substantially higher compared to that for platinum produced without PIM. Data for ESA and for catalytic activity are also summarised in Table 2. Note that the ESA relative to the geometric surface area of the electrode reaches unity at about 1-2 μg cm^{-2}. That is a 1-2 μg cm^{-2} deposit offers a platinum surface similar to a bare platinum electrode.

Table 2. Summary of film deposits in terms of specific electrochemical surface area (ESA), ESA relative to geometric surface area, and methanol oxidation peak currents (see below).

Amount of Pt / μg (on a 15 mm × 15 mm ITO)	0.9	1.3	2.3	5.4	9.8	39	97.5
ESA / $m^2\ g^{-1}$	10.6	38.0	78.4	84.5	7.5	4.1	1.6
ESA [a] / $m^2\ m^{-2}$	0.04	0.23	0.83	2.07	0.32	0.71	0.67
I_{peak} [b] / uA	85	249	1675	3827	665	1353	1352
i_{peak} [b] /A m^{-2}	0.38	1.11	7.44	17.0	2.96	6.01	6.01
Specific catalytic current / A g^{-1}	93	191	728	708	68	35	14

[a] area of platinum per geometric surface area of the electrode

[b] anodic peak current for 1 M methanol in 0.1 M $HClO_4$ during forward scan with 50 mV s^{-1} scan rate (see Figure 7).

3.4. Electrocatalytic Methanol Oxidation

Next, the reactivity of Pt@cPIM towards methanol oxidation was investigated. Small molecule [44,45] and in particular methanol oxidation to CO_2 (equation 2) has been extensively studied as a fuel cell process [46,47]. Platinum is commonly employed as catalyst component in methanol fuel cell devices [48].

$$CH_3OH(aq) \rightarrow CH_2O(aq) + 2\ H^+(aq) + 2\ e^-(m) \quad (2a)$$

$$CH_2O(aq) \rightarrow HCOOH(aq) + 2\ H^+(aq) + 2\ e^-(m) \quad (2b)$$

$$HCOOH(aq) \rightarrow CO_2(aq) + 2\ H^+(aq) + 2\ e^-(m) \quad (2c)$$

Figure 7A shows cyclic voltammetry data for the oxidation of 1 M methanol in aqueous 0.1 M $HClO_4$ at "thin film" Pt@cPIM catalyst with (i) 0.9, (ii) 1.3, (iv) 2.3, and (v) 5.4 μg Pt (this refers to the calculated weight of platinum metal not the composite). For comparison, trace (iii) shows data for a 39 μg Pt deposit without PIM support. Figure 7B shows data for only platinum deposited from precursor onto ITO. The inset shows a plot correlating the peak current for methanol oxidation with the amount of Pt in Pt@cPIM. At substantially lower loading with Pt the Pt@cPIM catalyst performs substantially better. Figure 7E compares catalytic current per gram of platinum to give a measure of specific catalytic efficiency (mass activity based on the forward oxidation peak and the weight of platinum deposit). A loading of 2.3 μg platinum appears to give the most effective methanol oxidation catalysts.

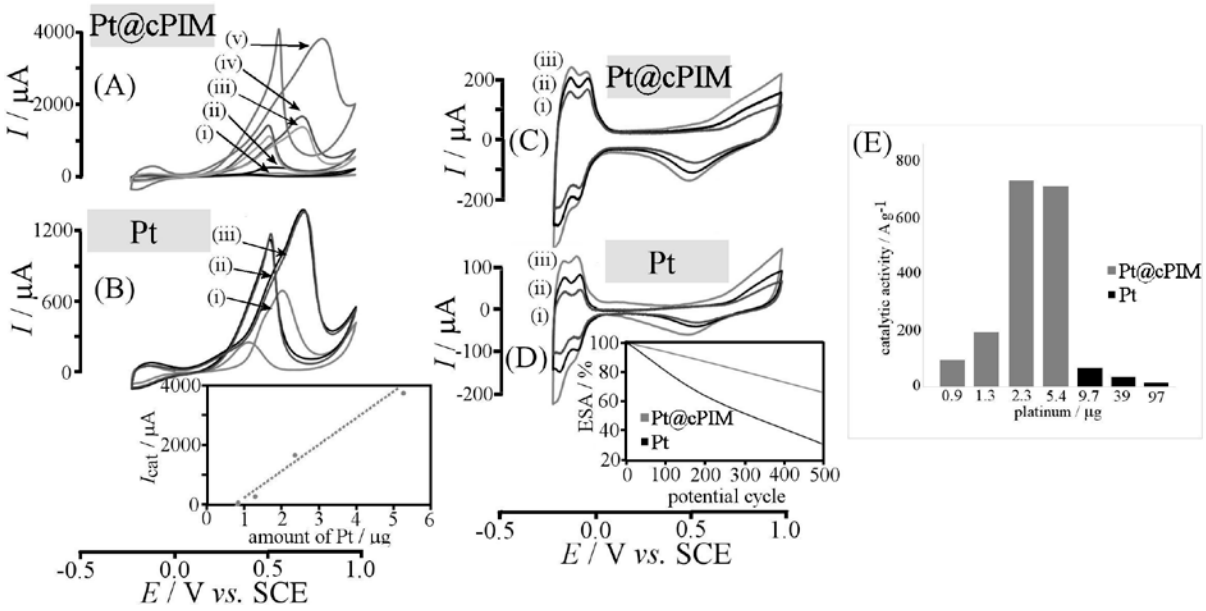

Figure 7. Cyclic voltammograms (scan rate 50 mVs^{-1}) for the oxidation of 1 M methanol in 0.1 M perchloric acid (A) at thin film Pt@cPIM with (i) 0.9, (ii) 1.3, (iv) 2.3, and (v) 5.4 μg Pt and (iii) 39 μg pure Pt and (B) at pure Pt deposits for (i) 9.7, (ii) 39, and (iii) 97 μg Pt. Inset shows catalytic methanol oxidation current versus amount of Pt for thin film Pt@cPIM. (C) Accelerated degradation testing (multi-cycle voltammograms with scan rate 50 mVs^{-1}) performed in 0.1 M perchloric acid for Pt@cPIM and (D) for pure Pt deposit. The inset shows the loss of active platinum surface area. (E) Plot of the specific mass activity (forward oxidation peak current divided by platinum weight) versus amount of Pt for different types of electrodes on ITO.

Additional experiments were performed to investigate the accelerated degradation of platinum catalyst under conditions of continuous potential cycling in aqueous 0.1 M $HClO_4$ (Figure 7C and 7D). Over 500 consecutive potential cycles the Pt@cPIM catalyst performs better (ca. 30 % loss of Pt activity) compared to the directly deposited Pt (ca. 70 % loss of Pt activity).

3.5. Electrocatalytic Glucose Oxidation

Glucose oxidation occurs on platinum electrode surfaces (mainly on catalytically active 100 oriented surfaces [49]) at relatively negative potentials within the hydrogen UPD region. The reaction mechanism is complex, but the main process has been suggested to be associated with a 2-electron transformation from glucose to gluconic acid or gluconolactone [50] (equation 3).

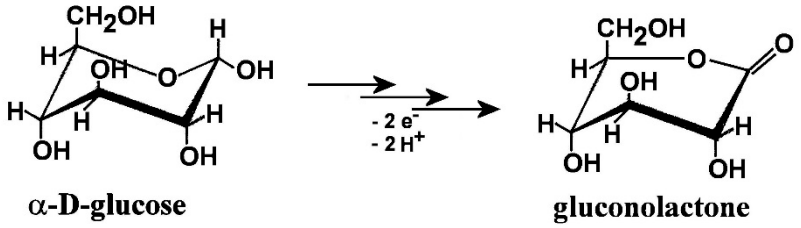

α-D-glucose gluconolactone

(3)

Figure 8A shows cyclic voltammetry data for the oxidation of 10 mM glucose in 0.1 M phosphate buffer pH 7 as a function of scan rate. A first oxidation peak is observed at -0.4 V vs. SCE consistent with literature reports [51]. This oxidation peak seems to originate from the (111)×(100) UPD region which in turn implies that hydrogen adsorption onto the platinum surface is an intermediate reaction step in the process described by equation 3. In Figure 8B data obtained at a bare 2 mm diameter Pt disk electrode is shown and very similar features are observed. Figure 8C and 8D report the effect of changing the glucose concentration over a

range from 2 to 14 mM in 0.1 M phosphate buffer pH 7. Well-defined peak currents are detected that correlate with glucose concentration up to approximately 10 mM. Beyond this point the current becomes independent of the glucose concentration due to a lack of reactive surface sites. Both Pt@cPIM and bare platinum exhibit very similar trends when currents are normalised according to surface area (ESA). The difference in relative magnitude of the catalytic currents (ca. 1:100) at bare platinum and Pt@cPIM can be explained based on the electrochemically active surface area (ESA), which is ca. 4.3 cm^2 for thick film Pt@cPIM compared to 0.04 cm^2 for a 2 mm diameter platinum disk.

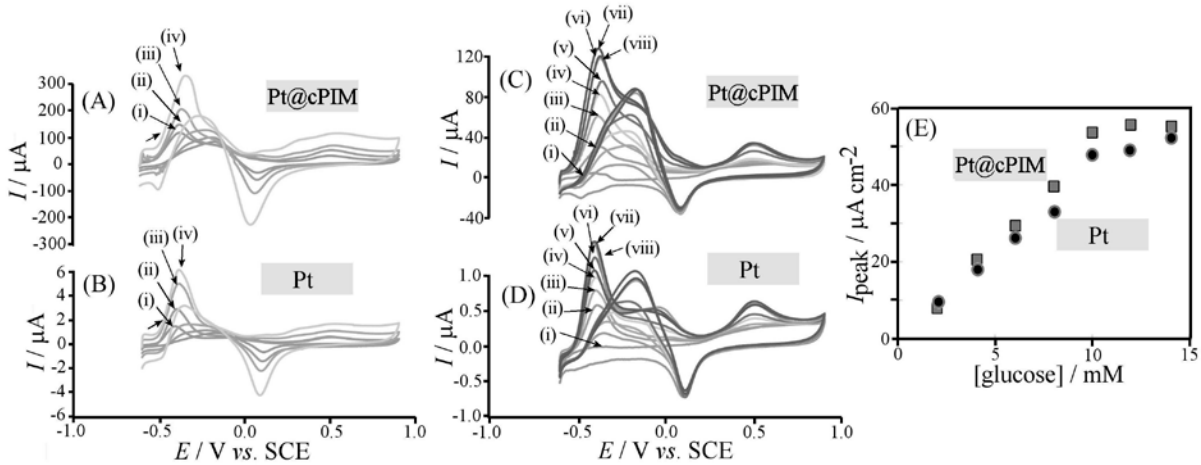

Figure 8. Cyclic voltammograms (scan rate (i) 5, (ii) 10, (iii) 20, (iv) 50 mVs^{-1}) for the oxidation of 10 mM glucose in 0.1 M phosphate buffer pH 7 (A) at a thick film Pt@cPIM electrode and (B) at a bare 2 mm diameter Pt disk electrode. Next, cyclic voltammograms for the oxidation of (i) 0, (ii) 2, (iii) 4, (iv) 6, (v) 8, (vi) 10, (vii) 12, (viii) 14 mM glucose in 0.1 M phosphate buffer pH 7 at (C) thick film Pt@cPIM and (D) a bare 2 mm diameter Pt disk electrode. (E) Plot of the normalised peak current density for glucose oxidation (based on ESA) versus glucose concentration.

The oxidation of glucose on platinum is known to be very sensitive to poisons such as chloride [52,53] and even phosphate. The effect of adding chloride is demonstrated in Figure 9A and 9B for Pt@cPIM and for bare Pt, respectively. Both types of catalyst show substantial loss of activity in the presence of chloride. This needs to be taken into consideration in particular when

using SCE reference electrodes, which tend to leak some chloride with time. In addition, phosphate buffer concentration effects the catalyst performance. Figure 9C and 9D show data for the oxidation of glucose in (i) 1.0, (ii) 0.1, and (iii) 0.01 M phosphate buffer pH 7. Both types of electrodes show similar trends with improved catalysis at lower phosphate buffer concentration.

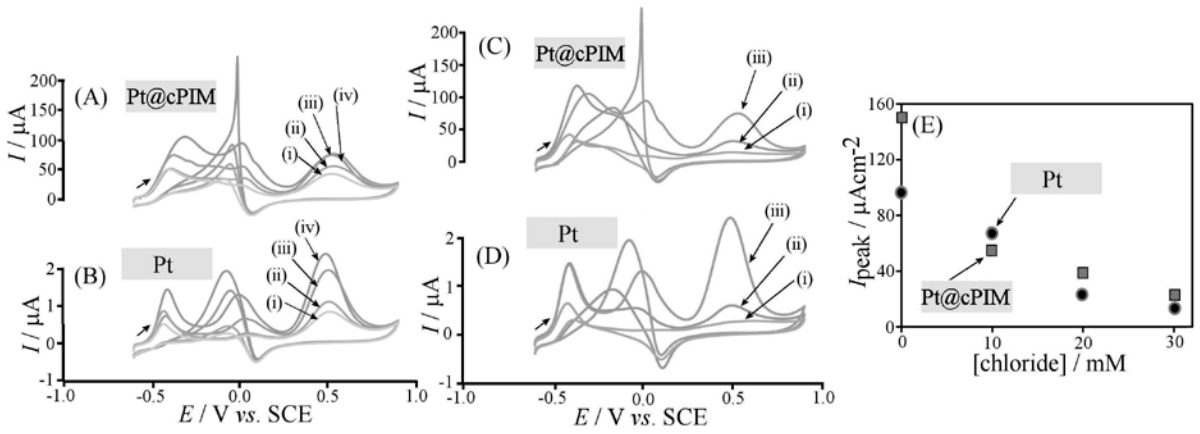

Figure 9. Cyclic voltammograms (scan rate 50 mVs^{-1}) for the oxidation of 10 mM glucose in 0.1 M phosphate buffer pH 7 in the presence of (i) 30, (ii) 20, (iii) 10, (iv) 0 mM chloride (NaCl) at (A) thick film Pt@cPIM and (B) bare 2 mm diameter platinum. Next, cyclic voltammograms (scan rate 50 mVs^{-1}) for the oxidation of 10 mM glucose in aqueous (i) 1.0 M, (ii) 0.1 M, (iii) 0.01 M phosphate buffer pH 7 at (C) thick film Pt@cPIM and (D) bare 2 mm diameter platinum disk. (E) Plot of the catalytic glucose oxidation current peak density (based on ESA) versus chloride concentration.

Based on these data, it can be suggested that the microporous cPIM catalyst support for both thick film and thin film cases offers (i) sufficient electrical conductivity to allow catalysis at platinum nanoparticles, (ii) negligible surface blocking effects for embedded nanoparticles, and (iii) sufficient porosity to allow oxygen, methanol, glucose and similar small molecules access to the embedded catalyst nanoparticles.

4. Conclusion

It has been demonstrated that PIM-EA-TB can be employed to immobilise a $PtCl_6^{2-}$ precursor for platinum by simple absorption from aqueous solution. Gentle vacuum carbonization then allows platinum nanoparticle catalyst of typically 1.0-2.5 nm diameter to be formed. The substrate is converted to a microporous hetero-carbon with the ability to conduct electrons and without the problem of blockage of catalytic sites on platinum. Three types of relevant redox processes were investigated: (i) the reduction of oxygen, (ii) the oxidation of methanol and (iii) the oxidation of glucose. For each case, good performance of the Pt@cPIM nano-catalyst is observed. A coverage of typically 1 μg cm^{-2} of Pt provided by Pt@cPIM appears to be as catalytically reactivity as bare platinum. This estimate can be compared to the geometric area calculated for an amount of platinum of ~ 1 μg cm^{-2} in the form of platinum nanoparticles of 2 nm diameter. This would indeed result in approximately 1 cm^2 geometric surface area. Therefore cPIM-Pt appears to provide *maximum* utilisation with all particles accessible and active in the molecularly rigid host material. At this stage, many experimental parameters remain unexplored and further study of platinum loading, carbonization conditions, and the effects introduced by different types of PIMs will be necessary. Powder samples will have to be prepared and applied as inks in order to allow more quantitative comparison to commercial standard catalysts.

We anticipate that the vacuum carbonization of PIMs with a range of different catalyst precursors will provide a general methodology for the production of high performance catalysts for various applications in electrochemistry. Instead of directly coating electrodes with films of PIM precursors, it will be beneficial to prepare bulk catalyst materials, which are then employed as an ink to apply to suitable electrode surfaces. The rigidity in the molecular

backbone of PIMs ensures minimal loss of catalyst surface activity, whilst high temperature carbonization allows the metal catalyst to form and restructures the matrix to an electrically conducting but still microporous substrate. Further work is planned to explore other types of reactions and applications.

Acknowledgements

Y.R. thanks the University of Bath for a fee waiver and the China Scholarship Council for a PhD stipend. D.H. thanks the Royal Society for a Newton International Fellowship. F.M. and N.B.M. thank the Leverhulme Foundation for financial support (RPG-2014-308: "New Materials for Ionic Diodes and Ionic Photodiodes").

References

1. H. Mistry, A.S. Varela, S. Kuhl, P. Strasser, B.R. Cuenya, Nat. Rev. Mater. **1**, 16009 (2016)
2. M. Zhou, S.J. Guo, ChemCatChem, **7**, 2744 (2015)
3. Y. Xu, B. Zhang, Chem. Soc. Rev. **43**, 2439 (2014)
4. S. Sharma, B.G. Pollet, J. Power Sources **208**, 96 (2012)
5. J. Biener, M. Stadermann, M. Suss, M.A. Worsley, M.M. Biener, K.A. Rose, T.F. Baumann, Energy Environm. Sci. **4**, 656 (2011)
6. W. Xia, A. Mahmood, R.Q. Zou, Q. Xu, Energy Environm. Sci. **8**, 1837 (2015)
7. L. Liu, Y.P. Zhu, M. Su, Z.Y. Yuan, ChemCatChem **7**, 2765 (2015)
8. C.R. Kim, T. Uemura, S. Kitagawa, Chem. Soc. Rev. **45**, 3828 (2016)
9. Q. Li, N. Mahmood, J.H. Zhu, Y.L. Hou, S.H. Sun, Nano Today **9**, 668 (2014)
10. P. Xu, X.J. Han, B. Zhang, Y.C. Du, H.L. Wang, Chem. Soc. Rev. **43**, 1349 (2014)
11. H.L. Fan, W.Z. Shen, ChemSusChem **8**, 2004 (2015)

12. Z.L. Xie, D.S. Su, Europ. J. Inorg. Chem. 1137 (2015)
13. J. Yin, L. Wang, P. Yu, L. Zhao, C.G. Tian, B.J. Jiang, D.D. Zhao, W. Zhou, H.G. Fu, ChemElectroChem **2**, 1813 (2015)
14. Y.Q. Cao, J.W. Zhang, Y. Yang, Z.R. Huang, N.V. Long, M. Nogami, J. Nanosci. Nanotechnol. **14**, 1194 (2014)
15. L. Su, W.Z. Jia, C.M. Li, Y. Lei, ChemSusChem **7**, 361 (2014)
16. R.N. Singh, R. Awasthi, C.S. Sharma, Internat. J. Electrochem. Sci. **9**, 5607 (2014)
17. A. Brouzgou, P. Tsiakaras, Topics Catal. **58**, 1311 (2015)
18. M.X. Wu, T.L. Ma, J. Phys. Chem. C **118**, 16727 (2014)
19. S. Marini, P. Salvi, P. Nelli, R. Pesenti, M. Villa, M. Berrettoni, G. Zangari, Y. Kiros, Electrochim. Acta **82**, 384 (2012)
20. E. Antolini, Appl. Catal. B-Environm. **181**, 298 (2016)
21. L. Li, L.P. Hu, J. Li, Z.D. Wei, Nano Res. **8**, 418 (2015)
22. D.P. He, Y.Y. Rong, Z.K. Kou, S.C. Mu, T. Peng, R. Malpass-Evans, M. Carta, N.B. McKeown, F. Marken, Electrochem. Commun. **59**, 72 (2015)
23. D.P. He, Y.Y. Rong, M. Carta, R. Malpass-Evans, N.B. McKeown, F. Marken, RSC Adv. **6**, 9315 (2016)
24. W. Xia, A. Mahmood, Z.B. Liang, R.Q. Zou, S.J. Guo, Angew. Chem., Int. Ed. **55**, 2650 (2016)
25. A. Afraz, A.A. Rafati, A. Hajian, M. Khoshnood, Electrocatalysis **6**, 220 (2015)
26. T. Xue, Z.P. Sun, L. Wei, X. Wang, J.M. Lee, Int. J. Hydrogen Energy **38**, 2754 (2013)
27. Y.Y. Rong, D.P. He, A. Sanchez-Fernandez, C. Evans, K.J. Edler, R. Malpass-Evans, M. Carta, N.B. McKeown, T.J. Clarke, S.H. Taylor, A.J. Wain, J.M. Mitchels, F. Marken, Langmuir **31**, 12300 (2015)
28. N.B. McKeown, P.M. Budd, Chem. Soc. Rev. **35**, 675 (2006)
29. N.B. McKeown, P.M. Budd, Macromolecules **43**, 5163 (2010)
30. N.B. McKeown, P.M. Budd, K.J. Msayib, B.S. Ghanem, H.J. Kingston, C.E. Tattershall, S. Makhseed, K.J. Reynolds, D. Fritsch, Chem. European J. **11**, 2610 (2005)
31. S. Kim, Y.M. Lee, Prog. Polymer Sci. **43**, 1 (2015)
32. Y.Y. Rong, R. Malpass-Evans, M. Carta, N.B. McKeown, G.A. Attard, F. Marken, Electrochem. Commun. **46**, 26 (2014)

33. E. Madrid, Y.Y. Rong, M. Carta, N.B. McKeown, R. Malpass-Evans, G.A. Attard, T.J. Clarke, S.H. Taylor, Y.T. Long, F. Marken, Angew. Chem. Int. Ed. **53**, 10751 (2014)
34. Y.Y. Rong, R. Malpass-Evans, M. Carta, N.B. McKeown, G.A. Attard, F. Marken, Electroanalysis **26**, 904 (2014)
35. M. Carta, R. Malpass-Evans, M. Croad, Y. Rogan, J.C. Jansen, P. Bernardo, F. Bazzarelli, N.B. McKeown, Science **339**, 303 (2013)
36. Y. Rogan, R. Malpass-Evans, M. Carta, M. Lee, J.C. Jansen, P. Bernardo, G. Clarizia, E. Tocci, K. Friess, M. Lancd, N.B. McKeown, J. Mater. Chem. A **2**, 4874 (2014)
37. J.P. Xie, Q.B. Zhang, W.J. Zhou, J.Y. Lee, D.I.C. Wang, Langmuir **25**, 6454 (2009)
38. A. Drelinkiewicz, J.W. Sobczak, E. Sobczak, M. Krawczyk, A. Zieba, A. Waksmundzka-Gora, Mater. Chem. Phys. **114**, 763 (2009)
39. J.M. Kinyanjui, R. Harris-Burr, J.G. Wagner, N.R. Wijeratne, D.W. Hatchett, Macromolecules **37**, 8745 (2004)
40. M.H. Shao, Q.W. Chang, J.P. Dodelet, R. Chenitz, Chem. Rev. **116**, 3594 (2016)
41. V. Stamenkovic, N.M. Markovic, P.N. Ross, J. Electroanal. Chem. **500**, 44 (2001)
42. T. Biegler, D.A.J. Rand, R. Woods, J. Electroanalytical Chem. **29**, 269 (1971)
43. C.E. Hotchen, G.A. Attard, S.D. Bull, F. Marken, Electrochim. Acta **137**, 484 (2014)
44. J. Jiang, A. Kucernak, J. Electroanal. Chem. **543**, 187 (2003)
45. J. Jiang, A. Kucernak, J. Electroanal. Chem. **533**, 153 (2002)
46. J.N. Tiwari, R.N. Tiwari, G. Singh, K.S. Kim, Nano Energy **2**, 553 (2013)
47. D.S. Falcao, V.B. Oliveira, C.M. Rangel, A.M.F.R. Pinto, Renew. Sust. Energy Rev. **34**, 58 (2014)
48. Y.W. Lee, S. Cha, K.W. Park, J.I. Sohn, J. Kim, J. Nanomater. 273720 (2015)
49. A. Rodes, M.J. Llorca, J.M. Feliu, J. Clavilier, Anales Quimica **92**, 118 (1996)
50. S. Park, H. Boo, T.D. Chung, Anal. Chim. Acta **556**, 46 (2006)
51. Y. Holade, C. Morais, K. Servat, T.W. Napporn, K.B. Kokoh, Phys. Chem. Chem. Phys. **16**, 25609 (2014)
52. N. Job, M. Chatenet, S. Berthon-Fabry, S. Hermans, F. Maillard, J. Power Sources **240**, 294 (2013)
53. J. Weber, A.J. Wain, G.A. Attard, F. Marken, Electroanalysis (2016) DOI: 10.1002/elan.201600443.

Graphical Abstract: